Plasma Phys. Control. Fusion **50** (2008) 065019 (17pp) doi:10.1088/0741-3335/50/6/065019

# Effect of transverse density modulations on fast electron transport in dense plasmas

**A P L Robinson[1], R J Kingham[2], C P Ridgers[2] and M Sherlock[1]**

[1] Central Laser Facility, STFC Rutherford-Appleton Laboratory, Chilton, Didcot, Oxfordshire, OX11 0QX, UK
[2] Imperial College London, Blackett Laboratory, Prince Consort Road, London, SW7 2BZ, UK

Received 10 December 2007, in final form 8 April 2008
Published 19 May 2008
Online at stacks.iop.org/PPCF/50/065019

**Abstract**
The effect of static transverse density modulations in the background plasma on fast electron transport is considered. It is shown that such density modulations can drive resistive filamentation in the fast electron beam when the target is sufficiently hot for the Spitzer resistivity to apply. The mechanism of magnetic field generation and filamentation is described both in terms of a semi-analytic model and a linearized analytic model. The results of numerical simulations showing the development of driven filamentation are presented.

(Some figures in this article are in colour only in the electronic version)

## 1. Introduction

The transport of relativistic electron beams (fast electrons) produced by the interaction of an ultraintense ($I\lambda^2 > 10^{18}\,\mathrm{W\,cm^{-2}}\mu\mathrm{m}^2$) laser pulse with a overdense plasma is a field that has been the subject of extensive research. A number of experiments have examined various aspects of fast electron transport [1–8], and this has been accompanied by efforts to develop suitable numerical [9–13] and analytic models [14–16].

A significant motivating factor behind these efforts is the fast ignition scheme for inertial confinement fusion [17]. The potential for laser-irradiated foils to be used as ion [18, 19] or x-ray sources [20] is another important motivation. The realization of these applications requires a good understanding of the physics of fast electron transport.

An important aspect of fast electron transport is the magnetic filamentation of a fast electron beam. This has been the subject of a number of recent investigations, both numerical [21–23] and analytical [24–27]. Usually this has been done for a collisionless (non-resistive) regime, although some valuable work has been done on the resistive regime, particularly by Gremillet *et al* [28]. Thus far, the effect of transverse (as opposed to the longitudinal effects examined in [27]) background density inhomogeneities have been neglected. By this we mean that there is a static inhomogeneity in the density of the background plasma. In this paper we examine the effect of transverse density modulations in the collisional/resistive regime

  

(specifically in a regime exhibiting Spitzer resistivity). It is shown that static background density modulations with an amplitude of 5% and a wavelength of several microns can produce strong filamentation in less than 1 ps by means of kinetic numerical simulations.

Fast electron transport often occurs under conditions in which it cannot be assumed that the background is perfectly homogeneous. Some slab targets can be intrinsically inhomogeneous, e.g. foam targets, or inhomogeneities can arise due to hydrodynamic effects caused by the laser pre-pulse. In a full fast ignition ICF scenario the fast electrons will propagate through a strongly inhomogeneous plasma. It may also be possible for the hydrodynamic response of the background plasma to the fast electron beam to create significant density modulations under certain conditions. All these considerations provide a strong motivation for a better understanding of the role of density inhomogeneities in fast electron transport.

It is proposed that static transverse background density modulations lead to a form of *driven* resistive filamentation. In qualitative terms this can be seen by considering a perturbation consisting of a single column of higher density surrounded by an annulus of lower density in a hot, dense plasma. Even if the fast electron current density parallel to these modulations is fairly uniform, the denser column must heat up more slowly and the annulus must heat up faster, because the specific heat capacity is linearly proportional to density. In this hot plasma the Spitzer resistivity applies, $\eta \propto T_{\mathrm{b}}^{-3/2}$ (where $T_{\mathrm{b}}$ is the background temperature), so the troughs become increasingly less resistive compared with the crests. By then considering Faraday's law, $\partial_t \boldsymbol{B} = -\nabla \times \boldsymbol{E}$, one sees that this must generate magnetic field which pushes fast electrons into the crest. If this magnetic field then modulates the fast electron current density, then there is the potential for resistive filamentation.

This paper is organized as follows: first the proposed mechanism is described in mathematical terms, specifically by both a semi-analytic 'rigid beam' model, and by a linearized analytic model that includes the response of the fast electron beam. The third section describes the numerical code employed in this paper. In the fourth section the simulation results are presented and interpreted.

## 2. Theory

In this section the filamentation mechanism is described in terms of: (a) a semi-analytic model that accounts for transverse inhomogeneity and strong heating, but not the response of the fast electron beam, and (b) an analytic model that includes the linear response of the fast electrons, but which assumes a beam that is initially uniform in the transverse direction and only weak heating of the background plasma. In both cases it is assumed that the dense plasma is initially at a sufficiently high temperature that the Spitzer resistivity should apply ( $>100$ eV for many solid density plasmas).

The semi-analytic estimate of the magnetic field growth uses the 'rigid beam' approach of Davies [15]. In this approach a *static* fast electron current density is assumed that varies only in $y$, i.e. $j_{\mathrm{f}} = j_{\mathrm{f}}(y)$. The model is 1D and assumes that the system is homogeneous in $x$ and $z$. The heating of the background plasma is described by

$$\frac{\partial T}{\partial t} = \frac{\eta j_x^2}{eCn_{\mathrm{e}}}, \tag{1}$$

where $T$ is in units of eV, and $C$ determines the specific heat capacity of the plasma (equal to $3/2$ for an ideal plasma). Thermal conduction is neglected in this model. The resistivity is given by the Spitzer resistivity,

$$\begin{aligned} &\eta = AT^{-3/2} \\ &\text{where} \quad A = 10^{-4} Z \ln \Lambda, \end{aligned} \tag{2}$$

and the magnetic field grows according to

$$\frac{\partial B_z}{\partial t} = \frac{\partial(\eta j_x)}{\partial y}. \tag{3}$$

Since both the background electron density and the fast electron current are static, one can immediately integrate equation (1) to obtain

$$T = \left(\frac{5}{2}\frac{A j_x^2 t}{eCn_e} + T_{\text{init}}^{5/2}\right)^{2/5}. \tag{4}$$

The magnetic field growth rates can now be derived straightforwardly. Starting by expanding equation (3) one obtains

$$\frac{\partial B_z}{\partial t} = \frac{A}{T^{3/2}}\frac{\partial j_x}{\partial y} - \frac{3}{2}\frac{A j_x}{T^{5/2}}\frac{\partial T}{\partial y}. \tag{5}$$

The $\partial T/\partial y$ term can be expanded by using equation (4) to yield

$$\frac{\partial B_z}{\partial t} = \frac{A}{T^{3/2}}\frac{\partial j_x}{\partial y} - 3\frac{A^2 j_x^2 t}{eCn_e T^4}\frac{\partial j_x}{\partial y} + \frac{3}{2}\frac{A^2 j_x^3 t}{eCn_e^2 T^4}\frac{\partial n_e}{\partial y}. \tag{6}$$

This equation can be interpreted as follows: the first term is the collimation/filamentation term that acts to generate magnetic field that pushes fast electrons towards regions of high current density, the second and third terms are the 'beam hollowing' terms that acts to generate magnetic field that pushes fast electrons towards regions of higher resistivity. However the third term is a special modification that is caused by the modulation of the background: since the regions of higher cold electron density should heat more slowly they should be more resistive than the surrounding troughs, and thus a magnetic field should be generated which drives fast electrons into the crests in the cold electron density. The background modulation will eventually affect all three terms.

The transverse density modulations are now introduced by specifying that

$$n_e(y) = n_0\left(1 + \delta\cos\left(\frac{2\pi y}{\lambda}\right)\right). \tag{7}$$

Note that $n_e \approx Zn_i$ for $\lambda \gg \lambda_D$, i.e. quasineutrality is assumed since the Debye length of the background plasma is much smaller than perturbations on the micrometre scale. The fast electron current density is given by

$$j_x(y) = j_0 \exp\left(-\frac{(y - y_b)^2}{2r_b^2}\right). \tag{8}$$

Now that the model is complete, it can be integrated for parameters that have relevance to ultraintense laser–solid interactions. Specifically we consider $Z \ln\Lambda = 26$, $C = 3/2$, $T_0 = 200\,\text{eV}$, $n_0 = 6 \times 10^{29}\,\text{m}^{-3}$, $\lambda = 5\,\mu\text{m}$ and $\delta = 0.05$. For the fast electron beam we take $j_0 = 5 \times 10^{15}\,\text{A m}^{-2}$, $r_b = 7\,\mu\text{m}$, and the beam is centred in the middle of the grid. The results of this calculation carried up to 500 fs and 1 ps are shown in figure 1.

It can be seen from figure 1, by comparing the top and bottom plots, that the magnetic field is certainly altered by the modulations to the background density. It can also be seen, from the middle plots, that the mechanism that is responsible for this is that embodied by the third term in equation (6). There is not sufficient modulation to the background temperature, and hence the resistivity, to strongly modulate the first term in equation (6). However, what needs to be addressed is whether these changes to the magnetic field are actually significant enough to alter the fast electron flow.

The response of the fast electrons can be considered in the first instance by a linearized analytic model. Certain assumptions must be made in order to make this tractable. In the

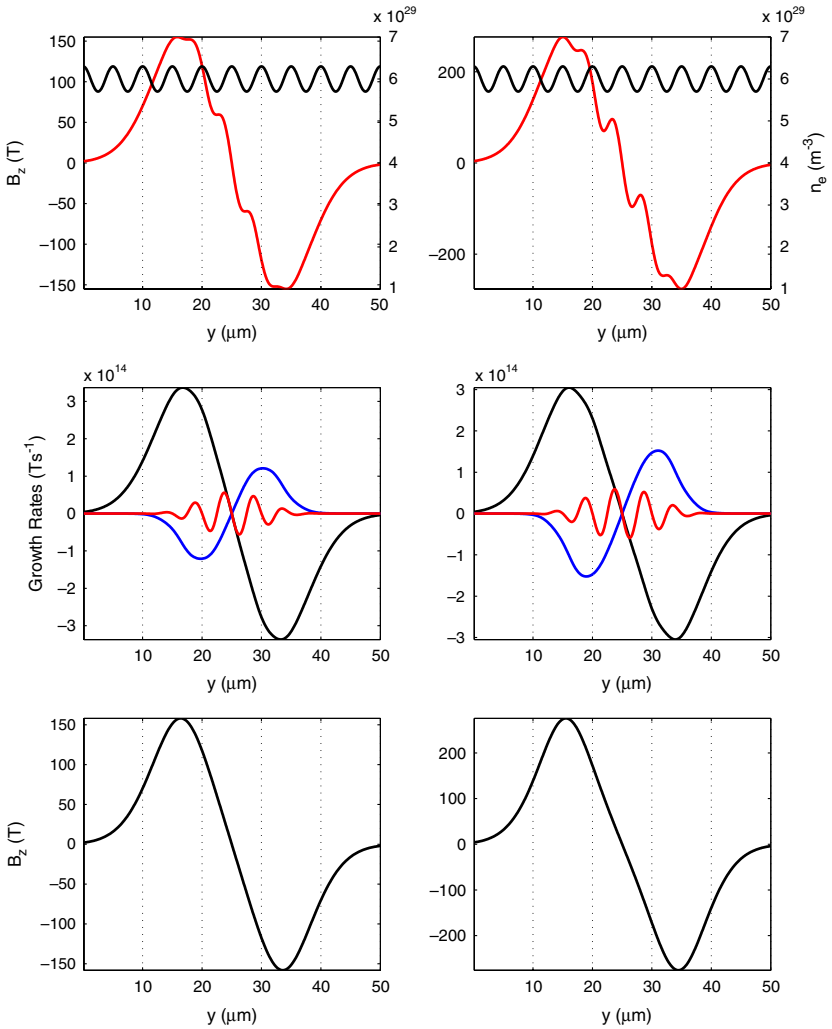


**Figure 1.** Results of integrating equation (6) up to 500 fs (left) and 1 ps (right). Top plots show $B_z$(T) (red) and $n_e$(m$^{-3}$) (sinusoidal; black). Middle plots show magnetic field growth rates for the first (largest amplitude; black), second (medium amplitude; blue) and third (smallest amplitude; red) terms in equation (6) separately. Bottom plots show $B_z$(T) at 500 fs (left) and 1 ps (right) without any density perturbation.

analytic model that is presented here, it is assumed that the fast electron beam is initially uniform in the transverse direction, and that the heating of the background plasma is weak (i.e. $T \approx T_{\rm init}$). The fast electrons are given a fluid description:

$$n_{\rm f} = n_{\rm f,0} + n_1(y,t), \tag{9}$$

$$u_{f,x} = u_{x,0}, \tag{10}$$

$$u_{f,y} = u_{y,1}(y,t). \tag{11}$$

Since $u_{f,y} \ll u_{f,x}$, $\gamma \approx (1 - u_{x,0}^2/c^2)^{-1/2}$. The fast electron beam is also assumed to have a small transverse energy spread, characterized by $T_{\rm f,\perp}$. The linearized fluid equations

that describe the fast electrons are

$$\frac{\partial n_1}{\partial t} + n_{\mathrm{f},0}\frac{\partial u_{y,1}}{\partial y} = 0, \tag{12}$$

$$\frac{\partial u_{y,1}}{\partial t} = \frac{e u_{x,0} B_z}{\gamma m_\mathrm{e}} - \frac{T_{\mathrm{f},\perp}}{\gamma m_\mathrm{e}}\frac{\partial n_1}{\partial y}. \tag{13}$$

This is coupled to equation (6), the second term of which is neglected in the limit of weak heating, and equation (7). The approximation $n_\mathrm{e}^2 = n_{\mathrm{e},0}^2$ is used in the denominator of the third term of equation (6). Solutions of the following form are now sought to this system of coupled equations: $n_1 = n_{\mathrm{f},0} N(t)\cos(k_\mathrm{p} y)$, $u_{y,1} = U(t)\sin(k_\mathrm{p} y)$, $B_z = B(t)\sin(k_\mathrm{p} y)$, where $k_\mathrm{p} = 2\pi/\lambda$. By combining equations (6), (7), (12) and (13), one can obtain a single ODE for $N$:

$$\frac{\partial^3 N}{\partial t^3} + \beta\frac{\partial N}{\partial t} - \alpha N = \mu t, \tag{14}$$

where

$$\alpha = \frac{e^2 u_{x,0}^2 n_{\mathrm{f},0} k_\mathrm{p}^2}{\gamma m_\mathrm{e}}\frac{A}{T^{3/2}}, \tag{15}$$

$$\beta = \frac{k_\mathrm{p}^2 T_{\mathrm{f},\perp}}{\gamma m_\mathrm{e}}, \tag{16}$$

$$\mu = \frac{e u_{x,0} k_\mathrm{p}^2 \delta}{\gamma m_\mathrm{e}}\left(\frac{3}{2}\frac{A^2 j_x^3}{e C n_{\mathrm{e},0} T^4}\right). \tag{17}$$

The solution to this ODE can be found straightforwardly by applying the constraints that $N(0) = 0$, $N'(0) = 0$ and $N''(0) = 0$:

$$N = C_1 \mathrm{e}^{gt} - \frac{\mu t}{\alpha} + C_2 \mathrm{e}^{-gt/2}\cos(ht) + C_3 \mathrm{e}^{-gt/2}\sin(ht), \tag{18}$$

where (defining $D = (\beta/3)^3 + (\alpha/2)^2$)

$$C_1 = -C_2 = \frac{\frac{\mu}{\alpha}}{\frac{9}{4}g + \frac{h^2}{g}}, \tag{19}$$

$$C_3 = \frac{\frac{3}{4}g^2 + h^2}{\frac{9}{4}g^2 h + h^3}\frac{\mu}{\alpha}, \tag{20}$$

$$g = (\alpha/2 + \sqrt{D})^{1/3} - (\sqrt{D} - \alpha/2)^{1/3}, \tag{21}$$

$$h = \frac{\sqrt{3}}{2}\left[(\alpha/2 + \sqrt{D})^{1/3} + (\sqrt{D} - \alpha/2)^{1/3}\right]. \tag{22}$$

Having obtained this solution, it can be plotted over a range of variables. In figure 2, $N$ is plotted at $t = 500\,\mathrm{fs}$ for a range of $\delta$, and $\lambda$ at $j_x = 10^{14}\,\mathrm{A\,m^{-2}}$ and $j_x = 10^{15}\,\mathrm{A\,m^{-2}}$. The background density is set at $6 \times 10^{29}\,\mathrm{m^{-3}}$ and the background temperature is set at 200 eV. The fast electron transverse temperature is set at $T_{\mathrm{f},\perp} = 20\,\mathrm{keV}$, $\gamma = 2$, $u_{x,0} \approx c$.

From equation (4) it is found that the temperature increase over 500 fs is only 3% for $j_x = 10^{15}\,\mathrm{A\,m^{-2}}$, so the weak-heating approximation is valid in this case. From figure 2 it can be seen that at $j_x = 10^{15}\,\mathrm{A\,m^{-2}}$ there is a wide range of $\lambda$ and $\delta$ over which the filamentation mode (of equation (18)) will grow to large amplitude (well beyond the linear regime in fact). In contrast, at $j_x = 10^{14}\,\mathrm{A\,m^{-2}}$ the mode grows only to $10^{-4}$ which is

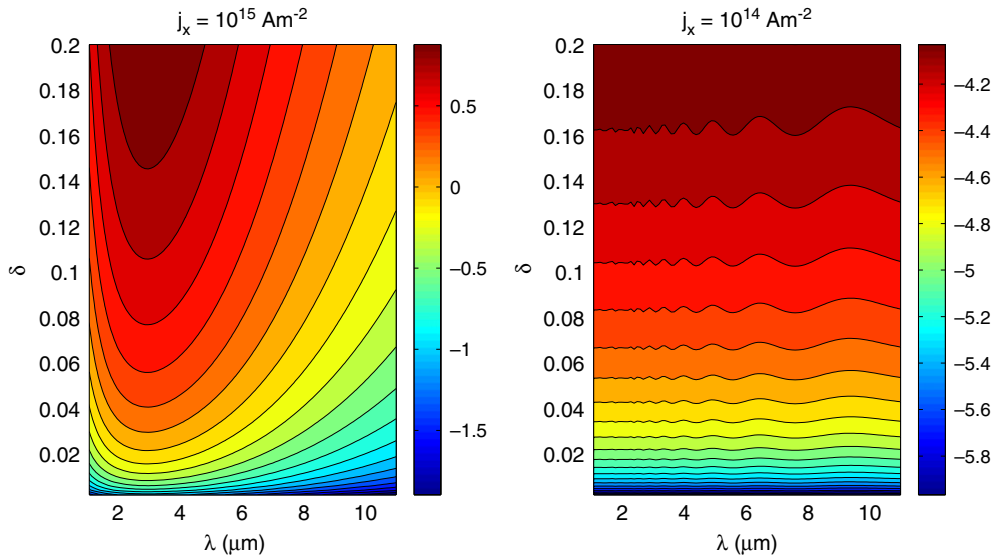


**Figure 2.** Plots of $\log_{10} N$ from equation (18) for $j_x = 10^{14}\,\mathrm{A\,m^{-2}}$ and $j_x = 10^{15}\,\mathrm{A\,m^{-2}}$ at 500 fs for a range of $\lambda$ and $\delta$. Other parameters are set at: $\gamma = 2$, $u_{x,0} = c$, $T_{\mathrm{f},\perp} = 20\,\mathrm{keV}$, $n_{\mathrm{e},0} = 6 \times 10^{29}\,\mathrm{m^{-3}}$, $T = 200\,\mathrm{eV}$.

fairly weak. Given the $j_x^3$ dependence in the third term of equation (6) this is not entirely unexpected. The fast electron current density close to the laser spot can be estimated by $f_{\mathrm{conv}} I_{\mathrm{laser}} = n_{\mathrm{f}} v_{\mathrm{f}} T_{\mathrm{f}}$. Assuming a conversion efficiency, $f_{\mathrm{conv}} > 0.1$, and a suitable fast electron temperature scaling (e.g. $T_{\mathrm{f}} = 0.511(\sqrt{1 + I\lambda^2/(1.38 \times 10^{18}\,\mathrm{W\,cm^{-2}\,\mu m^2})} - 1)\,\mathrm{MeV}$ [29]), one finds that the fast electron current density on injection is typically $10^{16}\,\mathrm{A\,m^{-2}}$. One therefore expects there to be a significant region in the target over which the fast electron current density will be sufficiently high to drive the growth of this filamentation mode in less than 1 ps.

## 3. Numerical model

The numerical code is the LEDA code which is a 2D hybrid Vlasov–Fokker–Planck (VFP) code [30]. This uses a KALOS-like [13] algorithm to describe the fast electrons, whilst the background electrons are given a hybrid description similar to the one in the hybrid code of Davies [10]. The distribution function of the fast electrons is expressed as a truncated spherical harmonic expansion with terms of the form $f_l^m(x, y, p) P_l^m(\cos\theta) \exp(\mathrm{i}m\phi)$. Substituting this expansion into the VFP equation yields a set of equations for the $f_l^m(x, y, p)$ coefficients. A brief description of the solution of these equations by means of the KALOS algorithm is given in [13, 31]. This code was previously used in an investigation of the 'structured collimator' concept [30], and the core elements of the version of the code used in this investigation does not differ significantly from the version employed in that work. Reflective boundary conditions are used in both $x$ and $y$.

The resistivity model used in this investigation is the Spitzer model, i.e. $\eta = 10^{-4} Z \ln\Lambda T^{-3/2}$, with an ideal specific heat capacity, and $Z \ln\Lambda = 26$, throughout. This models an Al target. The perturbation to the background density was specified using the

**Table 1.** Parameters employed in runs A–H.

| Run | L ($\mu$m) | $d$ ($\mu$m) | $\delta$ | $\lambda$ ($\mu$m) |
|---|---|---|---|---|
| A | 5 | 20 | 0.025 | 25 |
| B | 5 | 20 | 0.05 | 25 |
| C | 5 | 20 | 0.1 | 25 |
| D | 5 | 20 | 0.2 | 25 |
| E | 5 | 20 | 0.05 | 12.5 |
| F | 5 | 20 | 0.05 | 6.25 |
| G | 5 | 20 | 0.05 | 3.125 |
| H | *n/a* | *n/a* | *n/a* | *n/a* |

following formulae:

$$\begin{aligned} S_x &= \frac{1}{2}\left(1+\tanh\left(\frac{x-d}{L}\right)\right) \\ S_y &= \delta\cos\left(\frac{2\pi y}{\lambda}\right) \\ n_\mathrm{i} &= n_{\mathrm{i},0}(1+S_x S_y). \end{aligned} \tag{23}$$

This modulation to the background plasma density is completely static. In reality, no such perturbation can be completely static. It is however a very good approximation for two reasons. Firstly, as previously mentioned, $\lambda > 1\,\mu$m is being considered. This is much greater than the cold Debye length, which is typically less than 1 nm at solid density. Therefore, quasineutrality will be very well maintained. Secondly the thermal relaxation of the density perturbation occurs on a time-scale of $\lambda/c_\mathrm{s}$, where $c_\mathrm{s} = \sqrt{Zk_\mathrm{B}T/m_\mathrm{i}}$ is the sound speed in the plasma. For a temperature of 500 eV, $\lambda = 1\,\mu$m, and an ion charge to mass ratio of 1/2 this takes $\approx$7 ps. Therefore, provided the simulation time is limited to 1 ps, the use of a static density profile is justified. Since this will force magnetic fields to grow on the spatial scale of $\lambda$, according to the arguments presented in section 2, neglecting magnetic diffusion in the code must be addressed. The characteristic time for magnetic diffusion is given by $\mu_0 L^2/\eta$, where $L$ is characteristic scale length. Setting $L = 3\,\mu$m (the smallest $\lambda$ used in any simulation; see table 1), and noting that the highest resistivity is $\eta = 9.2\times10^{-7}\,\Omega\,$m, one determines a minimum characteristic diffusion time of 12 ps which is much greater than the simulation time of 1 ps.

The fast electrons are injected in the first spatial cell, at the left-hand end of the grid, and the 'laser' intensity is modelled by an energy flux of fast electrons

$$I = \beta I_0 \exp(-(y-y_\mathrm{m})^2/R^2), \tag{24}$$

which is constant over the injection time, $t_\mathrm{pulse}$. The parameter $R$ determines the extent of the region of fast electron injection, with the full width at half-maximum size of the spot being equal to $2R\sqrt{\ln 2}$. The fast electron temperature, $T_\mathrm{f}$, is determined by Beg's law [32] for $I_0 < 10^{19}\,\mathrm{W\,cm^{-2}}$, and by the scaling law of Wilks [29] for $I_0 > 10^{19}\,\mathrm{W\,cm^{-2}}$. The injected fast electron distribution function is specified to be

$$f_\mathrm{injected} \propto \cos^M\theta p^2 \exp\left(-c\sqrt{p^2+m_\mathrm{e}^2c^2}/k_\mathrm{B}T_\mathrm{f}\right). \tag{25}$$

This distribution is a relativistic Maxwellian which is beamed into the target. The degree of anisotropy is controlled by the $\cos^M\theta$ term, which is close to 1/2 when $\theta = 67^\circ/\sqrt{M}$ (a better approximation the larger $M$ is). Therefore $\theta_{1/2} = 67^\circ/\sqrt{M}$ is the half-maximum

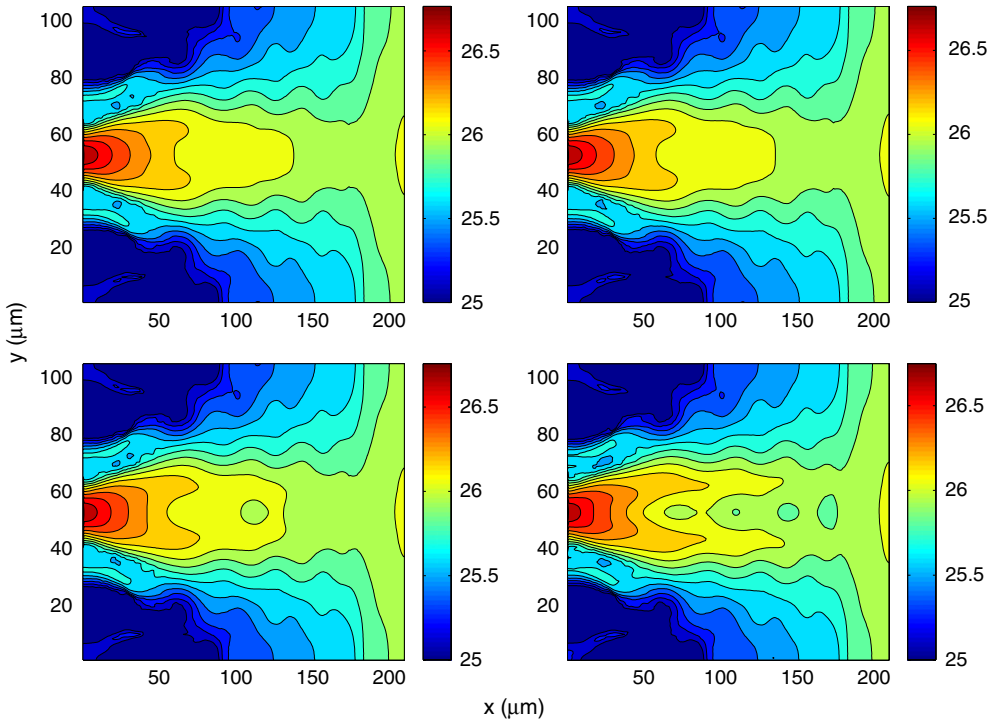


**Figure 3.** Plots of fast electron density ($\log_{10}(\mathrm{m}^{-3})$) at 800 fs in run A (top left), B (top right), C (bottom left) and D (bottom right).

angular spread of the injected electrons. The choice of divergence angle is taken primarily from experimental work [33] (supported by PIC simulations), which indicates that the full divergence angle of the electron beam between $I = 10^{19}$–$10^{20}\,\mathrm{W\,cm^{-2}}$ is 30 °–45 °.

In the standard run a uniform spatial grid with 280 cells in $x$, 140 cells in $y$ and a cell size of 0.75 $\mu$m was used. The momentum grid used 75 grid points and 22 harmonics were used in the expansion. The laser pulse was modelled by setting $I_0 = 5 \times 10^{19}\,\mathrm{W\,cm^{-2}}$, $R = 6\,\mu\mathrm{m}$ and $t_{\mathrm{pulse}} = 500$ fs. The chosen value of $I_0$ corresponds to $T_{\mathrm{f}} = 2.6$ MeV. The divergence angle was set to $M = 8 (\approx 24^\circ$ half angle), which is slightly greater than that indicated by experimental results (as discussed above). The laser absorption efficiency, $\beta$, was set to 0.3. The simulations were run up to 1 ps.

## 4. Results and discussion

### *4.1. Simulation results*

The effect of transverse density modulations was studied by carrying out a series of runs with an initial temperature of 200 eV. The parameters used in these runs (labelled A–H) are tabulated below. Note that H is a 'control run' where no density perturbations are present.

In these simulations, varying degrees of filamentation are observed, and this is evident in the fast electron density. The fast electron densities in runs A–D at 800 fs are shown in figure 3, and the fast electron densities in runs E–H at 800 fs are shown in figure 4. The fast electrons are injected from the LHS of the computational domain. The degree of filamentation

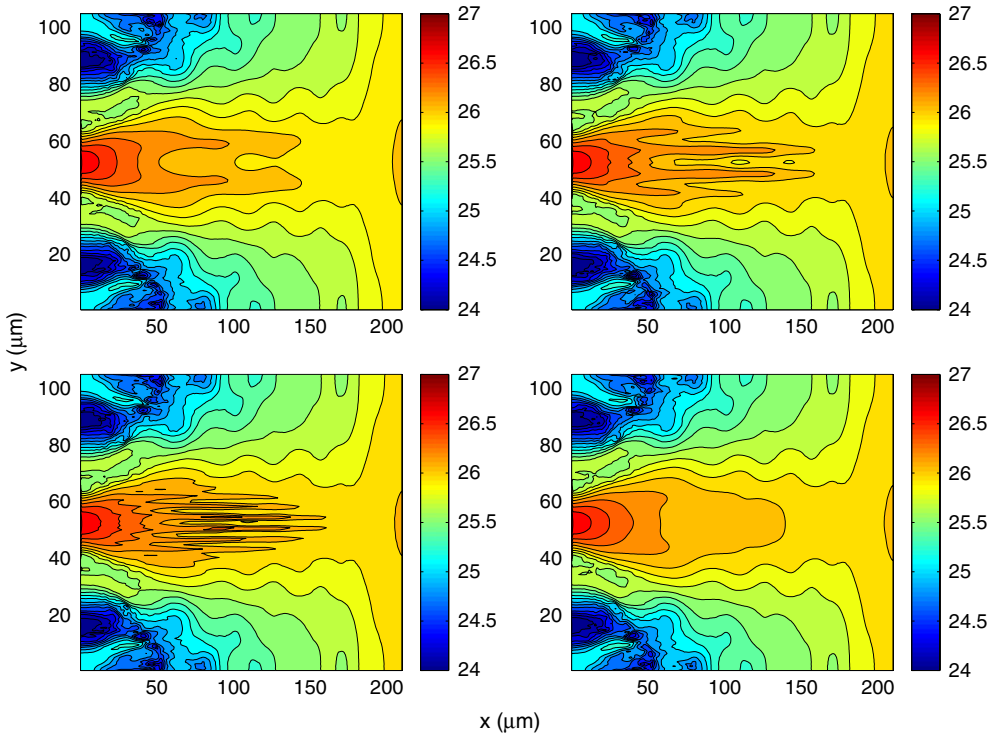


**Figure 4.** Plots of fast electron density ($\log_{10}(\mathrm{m}^{-3})$) at 800 fs in run E (top left), F (top right), G (bottom left) and H (bottom right).

becomes stronger at shorter modulation wavelengths and at larger $\delta$. This broadly agrees with the theoretical models (see figure 2).

This filamentation is clearly magnetic, as can be seen in the plots of the $B_z$ component of the magnetic flux density which are shown in figure 5 (for runs D–F). The filamentation wavelength observed in both the magnetic field and the fast electron density appears to be equal to the wavelength of the background density modulation. This is much clearer in line-outs of the numerical output (see figure 7). The background temperature and resistivity in runs D–F are shown in figure 6.

One can better understand these simulations by examining the line-outs (in $y$) of various parameters from a typical run alongside a line-out of the background ion density. Line-outs of $B_z$, $n_\mathrm{f}$, $T_\mathrm{b}$, and $j_{x,\mathrm{f}}$ in run E at 750 fs and $x = 60\,\mu$m are plotted in figure 7. Figure 7 clarifies what is shown in figure 4 in the sense that it clearly shows that both the fast electron density and current density are being channelled into the crests of the density profile. It also shows that a decollimating magnetic field has been generated in the central background density trough. These plots show that the nature of the filamentation conforms very strongly to predictions which are stated in section 2.

In summary, on examining this set of figures, it is clear that there is a magnetic filamentation effect that 'follows' the underlying pattern of the density modulations (from figures 3–5). By this we mean that the fast electrons filament along the crests of the background perturbation, and this enforces the characteristic length scale of the filamentation. As $\delta$ is increased, and $\lambda$ is decreased, the filamentation effect becomes stronger. When one examines some line-outs of

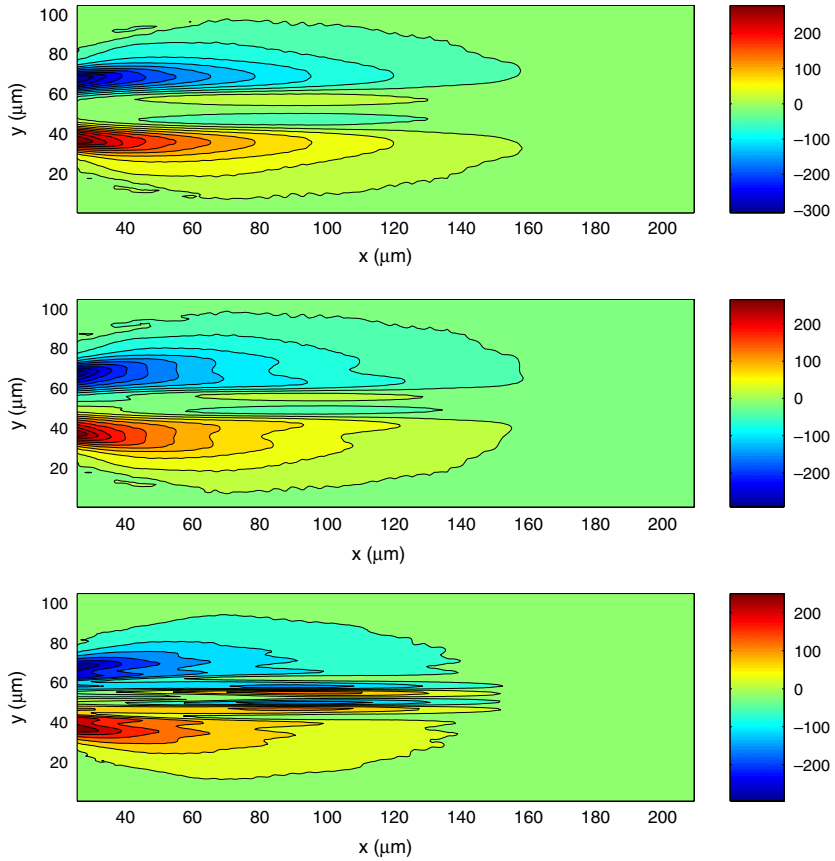


**Figure 5.** Plots of the $B_z$(T) component of the magnetic flux density at 800 fs in runs D (top), E (middle) and F (bottom).

various parameters it is clear that this seems to agree with the arguments and models presented in section 2, however further examination is required.

### *4.2. Intepretation*

In order to explain the observed filamentation of the fast electron beam, we will use run F as a 'case study'. The induction equation (i.e. equation (6)) can be written as $\boldsymbol{B} = \eta\nabla\times\boldsymbol{j}_\mathbf{f}+(\nabla\eta)\times\boldsymbol{j}_\mathbf{f}$. The first term of this expression corresponds to the first term in equation (6), and the second term corresponds to the sum of the second and third terms of equation (6). An outline of the proposed explanation for the observed filamentation can now be stated as follows: (i) The $\eta\nabla\times\boldsymbol{j}_\mathbf{f}$ term is dominant but it is modulated by the $(\nabla\eta)\times\boldsymbol{j}_\mathbf{f}$ term to produce a modulated magnetic field. (ii) This modulation of the magnetic field drives a modulation of the fast electron density and current density. (iii) There is an enhancement of the $\eta\nabla\times\boldsymbol{j}_\mathbf{f}$ magnetic field growth due to these modulations which cause them to grow rapidly due to positive feedback. Thus the filaments are produced, and they coincide with the 'ridges' in the background density.

By examining the magnetic field and the magnetic field growth rates due to both the $\eta\nabla\times\boldsymbol{j}_\mathbf{f}$ and the $(\nabla\eta)\times\boldsymbol{j}_\mathbf{f}$ term, which are shown at three different times in figure 8, one concludes that the first and last parts of the explanation are consistent with this information. Figure 8 indeed

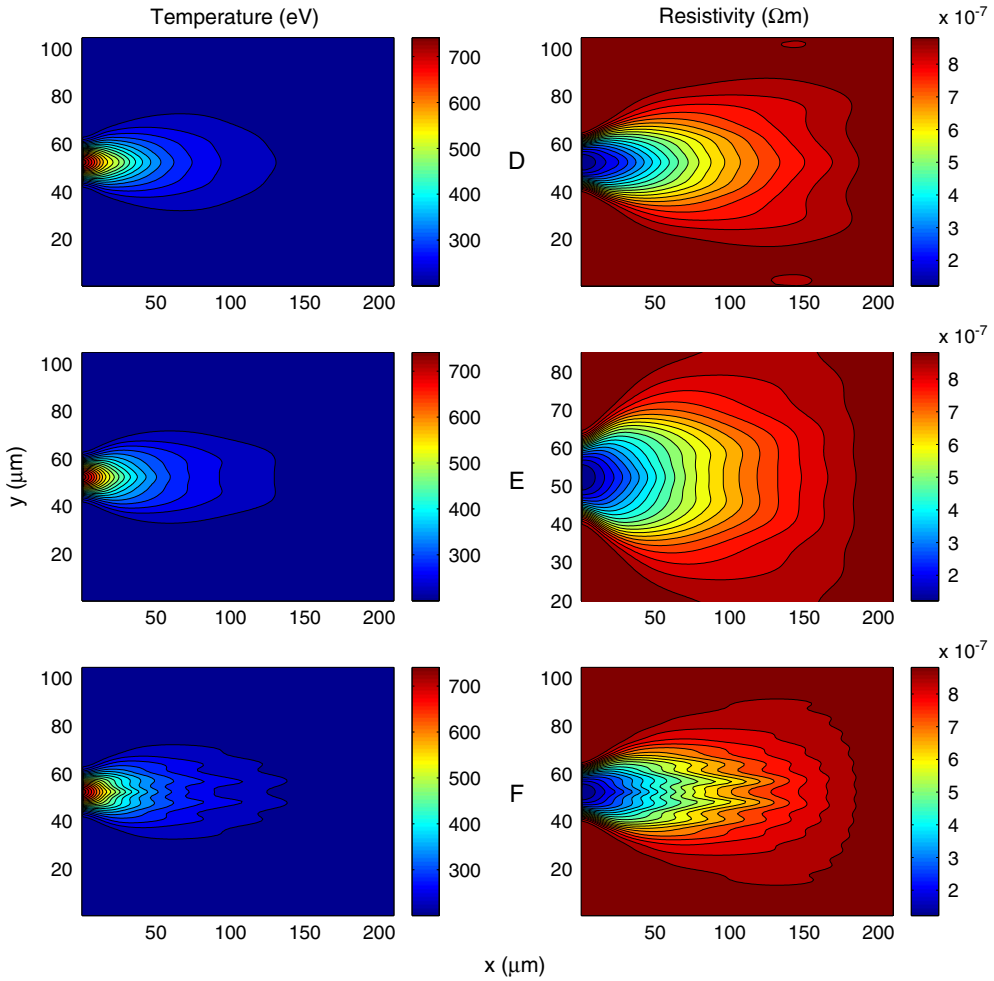


**Figure 6.** Plots of the background temperature (left) and resistivity (right) at 800 fs in runs D (top), E (middle) and F (bottom).

shows that the magnetic field growth is dominated by the $\eta\nabla\times\boldsymbol{j}_{\mathbf{f}}$ term. However at early times this magnetic field growth is modulated by the $(\nabla\eta)\times\boldsymbol{j}_{\mathbf{f}}$ term. At late times, once the beam is strongly filamented, the $\eta\nabla\times\boldsymbol{j}_{\mathbf{f}}$ term can generate the modulated magnetic field alone.

How does this relate to the predictions made by the models presented in section 2? At early times the 'rigid beam' model gives the correct insights into the physics. Specifically it predicts that $\eta\nabla\times\boldsymbol{j}_{\mathbf{f}}$ is dominant, but modulated by $(\nabla\eta)\times\boldsymbol{j}_{\mathbf{f}}$, which is exactly what is seen in the numerical simulations. Late in the simulations, the 'rigid beam' model does not correctly describe the physics, but this is obviously because the fast electron beam profile has been strongly changed due to filamentation (which clearly invalidates the assumption of a 'rigid beam'). The linearized analytic model must give some insight into the evolution at later times as that model effectively predicted that the modulation of the fast electron current density would be sufficient to modulate the $\eta\nabla\times\boldsymbol{j}_{\mathbf{f}}$ term, and that this would lead to exponential growth of the filaments. In qualitative terms the linearized analytic model and the simulations both show that this occurs; this is examined quantitatively in the following section.

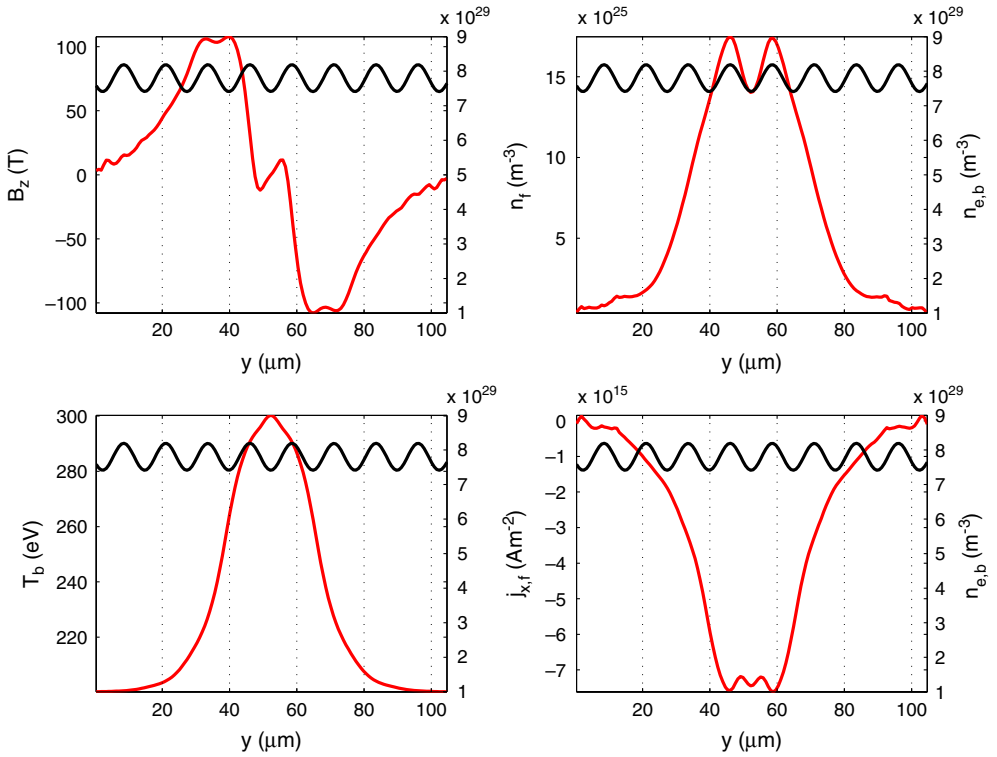


**Figure 7.** Plots of $B_z$ (top left), $n_\mathrm{f}$ (top right), $T_\mathrm{b}$ (bottom left), and $j_{x,\mathrm{f}}$ (bottom right) in run E at 750 fs and $x = 60\,\mu$m in red. Sinusoidal (black) lines are the background ion density for comparison.

Some explanation is required regarding the temperature profile shown in figure 6 which shows that the region that coincides with the filaments actually become hotter and hence less resistive than the surrounding material late in the simulation. This does not contradict the explanation that has been given. This can be seen by looking at the evolution of the temperature profile along $x = 75\,\mu$m in run F. This is shown in figure 9, along with the corresponding line-out of $B_z$. It is seen that at early times (250–500 fs) the central trough heats up more quickly than the nearby crests. It is this non-uniform heating that modulates the magnetic field in this time (cf figure 8). Only at late times (750 fs) when filamentation has already become very strong, do the filaments become much hotter than the surrounding material.

### *4.3. Growth rates*

These simulations cannot be directly compared with a standard linearized resistive filamentation theory. Such theories make a number of assumptions which are simply not valid in these numerical simulations. For example, Gremillet *et al* [28] assume that the transverse extent of the beam is infinite, that the plasma resistivity is constant and that the fast electrons are close to a monoenergetic beam in momentum space. Similar assumptions are made in the linearized theory presented in section 2. None of these apply to the simulations, so a *direct* comparison is not appropriate. Nonetheless some quantitative comparison between linear theory and the simulations can be attempted.

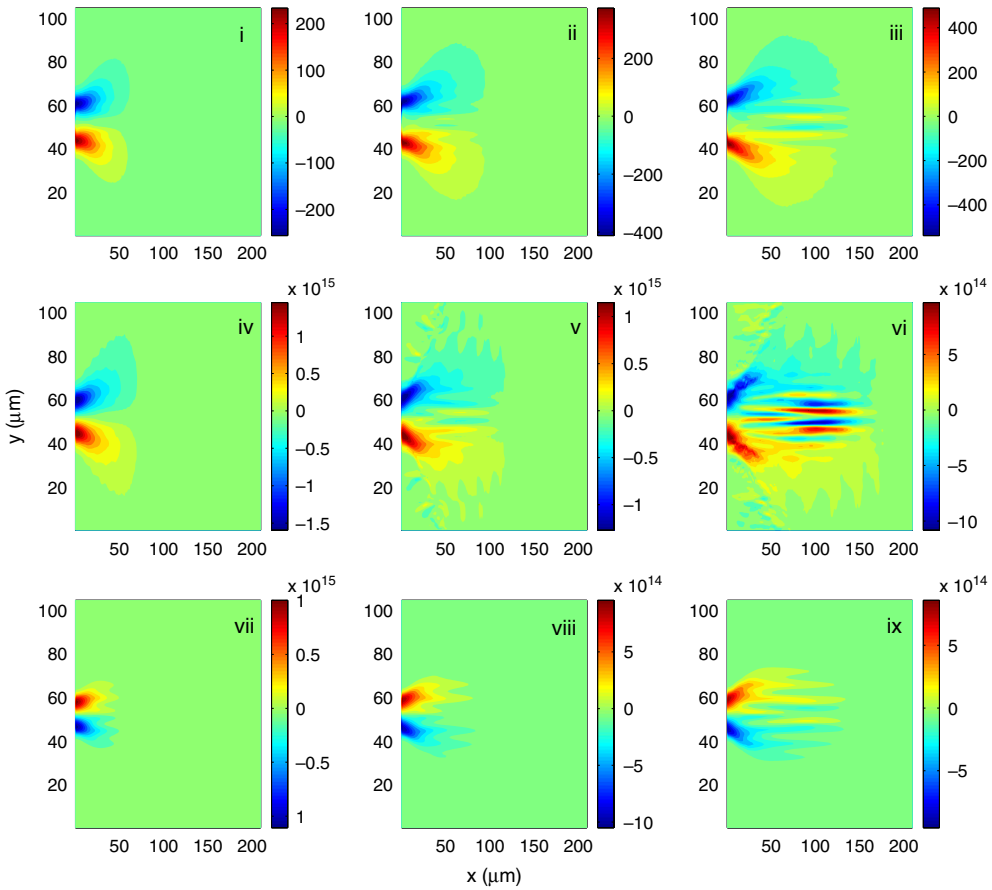


**Figure 8.** Plots of the $B_z$(T) component of the magnetic flux density (i)–(iii), plots of $\eta\nabla\times\boldsymbol{j}_\mathbf{f}$(T s$^{-1}$) (iv)–(vi), plots of $(\nabla\eta)\times\boldsymbol{j}_\mathbf{f}$(T s$^{-1}$) (viii)–(ix), at 250 fs, 500 fs and 750 fs, respectively in run F.

Obtaining a characteristic 'growth rate' of the filamentation in these simulations is not straightforward because of the inherent spatial inhomogeneity. In order to quantitatively analyse the filamentation we will consider the temporal evolution of the *de collimating* part in the magnetic field that grows near the central axis. Above the central axis this is a positive spike in $B_z$(see figure 9). The magnitude of this $B_z > 0$ spike ($B_z^*$) is plotted for $x = 75\,\mu$m in run F in figure 10. In order to appreciate the applicability of the linearized theory developed in section 2, the maximum fast electron current density and background temperature at $x = 75\,\mu$m in run F are plotted against time in figure 11.

Figure 10 shows that once this spike in the magnetic field appears it grows rapidly, but does not exhibit constant exponential growth. During the early growth of the spike (350–450 fs), the background temperature (210–230 eV) is still fairly close to its initial value (200 eV). The linearized weak-heating theory is most valid during this time, and when one plots the magnitude of the magnetic field predicted by this theory against the simulation results one finds that there is reasonable agreement. The choice of parameters being: $j_x = 6\times10^{15}\,\mathrm{A\,m^{-2}}$, $T = 200\,\mathrm{eV}$, $\gamma = 6$, $Z\ln\Lambda = 26$, $n_{\mathrm{e},0} = 6\times10^{29}\,\mathrm{m^{-3}}$ and $T_{\mathrm{f},\perp} = 100\,\mathrm{eV}$. The values of $\lambda$ and $\delta$ are the same as those for run F (see table 1). The analytic mode grows starting from $t = 400$ fs.

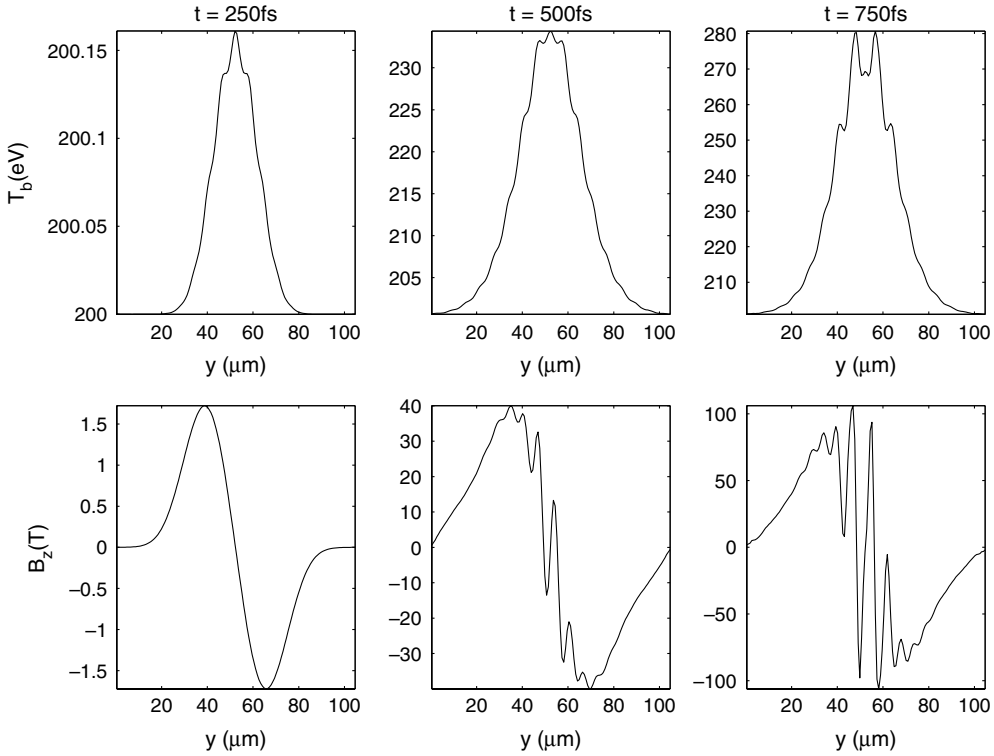


**Figure 9.** Background temperature and $B_z(T)$ along $x = 75\,\mu$m at 250, 500 and 750 fs in run F.

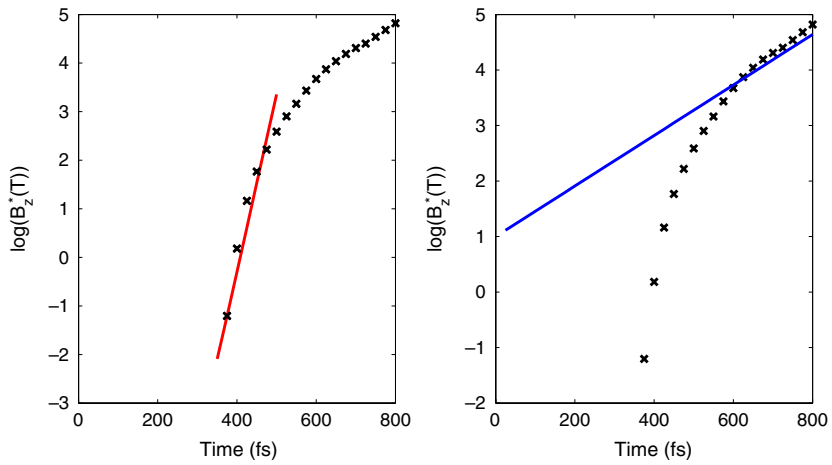


**Figure 10.** Growth of $B_z^*$ during run F (both plots). The solid red line in left-hand plot is the magnitude of the filamentation mode predicted by the linearized weak-heating theory (see text). The solid blue line in the right-hand plot corresponds to an e-folding time of 200 fs.

At late times however the spike grows more slowly than theory would predict for $T_{\mathrm{f},\perp} = 100$ eV. In figure 10 it is shown that an e-folding time of 200 fs matches the growth rate at late times. The linearized weak-heating theory predicts an e-folding time for appropriate parameters (similar to those given above, except that $T = 275$ eV, and $j_x = 8\times10^{15}$ A m$^{-2}$) and

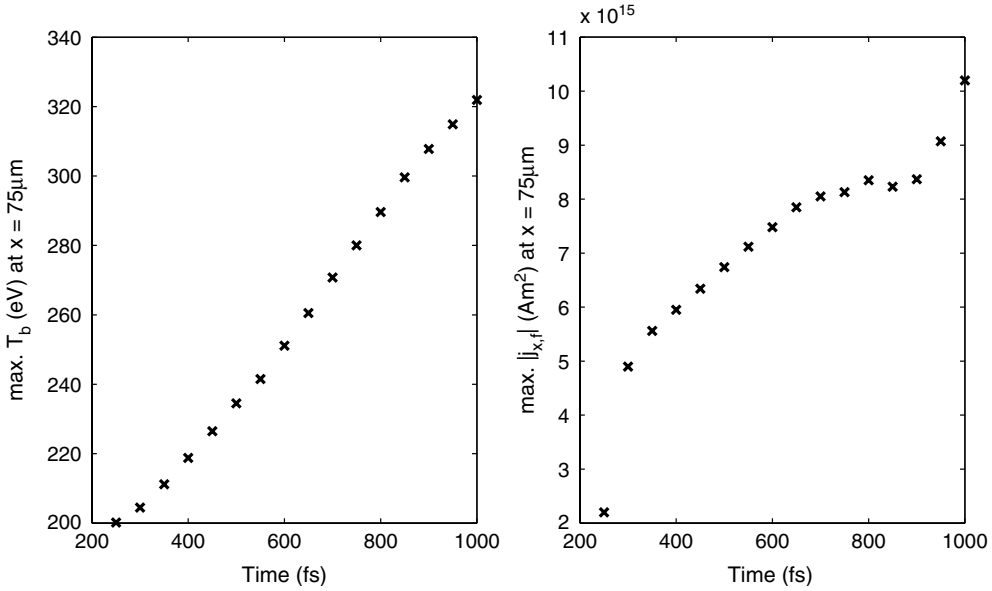


**Figure 11.** Maximum background temperature at $x = 75\ \mu$m in run F against time (left). Maximum $|j_{x,\mathrm{f}}|$ at $x = 75\ \mu$m in run F against time (right).

a much higher transverse fast electron temperature, $T_{\mathrm{f},\perp} = 300$ keV. This is sensible because at this point the filamentation has grown beyond the bounds of the linear approximation, the fast electrons are substantially deflected in the magnetic field, and the filamentation is beginning to saturate.

This procedure was repeated for runs E and G, and the comparison between the linearized weak-heating theory and the simulations is shown in figure 12. The same parameters were used in the analytic model, except that the wavelength was set to the value appropriate to the simulation. The comparison between the analytic theory and the simulation results is reasonable at early times.

The most important fact to emerge from this analysis is that there is reasonable agreement between the linearized weak-heating theory and the simulations during the early growth of the filamentation mode. This indicates that the analytic theory should be able to predict those regions of parameter space in which there is rapid growth of this filamentation mode.

## 5. Conclusions

In this paper we have described a new mechanism for driving resistive filamentation in the Spitzer regime. This is based on static transverse density modulations in the background plasma. Since this effectively modulates the specific heat capacity of the background plasma this leads to an additional magnetic field generation term as the background is heated by the drawing of a return current. This in turn modulates the magnetic field sufficiently to initiate filamentation. Once filamentation is initiated the generation of magnetic field through the standard resistive filamentation term, $\eta\nabla\times\boldsymbol{j}_{\mathbf{f}}$, causes the filamentation to grow.

Both a semi-analytic, 'rigid beam' model, and a linearized analytic model were used to study the magnetic field growth and filamentation under certain approximations. Kinetic numerical simulations performed using the LEDA code were then performed to verify that this

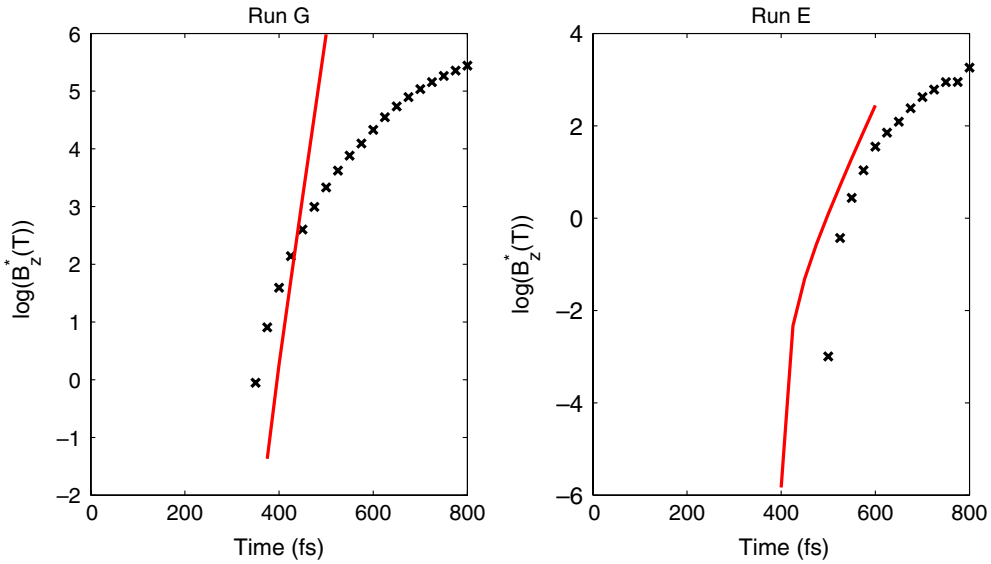


**Figure 12.** Growth of $B_z^*$ during runs G (left) and E (right). The solid red lines correspond to growth rate predictions made by the linearized weak-heating theory (see text). Solid lines are shifted due to starting the analytic mode growth at 400 fs. The bending of the solid line in the right-hand plot is due to the non-exponential terms in equation (18).

modulation did indeed initiate filamentation under more realistic conditions. It was found that an initial density modulation of 5% and several microns wavelength was sufficient to produce fairly strong filamentation in 1 ps. The growth rate of the filamentation mode observed in the simulations is in reasonable agreement with the growth rate predicted by the linearized analytic model.

This work has concentrated on the regime of Spitzer resistivity. In current laboratory experiments, targets are initially cold (a few eV due to pre-pulse). Even in solid targets that are at low temperatures an analogue of this mechanism should still operate. This is because the specific heat capacity is linearly proportional to density ($n_e T_e \pi^2 k_B^2 / 2E_F$ in a free electron gas), and because there is some variation of resistivity with temperature. However at low temperatures the resistivity can increase with temperature, which means that the magnetic field will act to push fast electrons into density troughs, not density crests, over this temperature range. Although detailed resistivity calculations have shown that the Spitzer resistivity applies at high temperatures [34], and the resistivity is thus independent of the plasma density, at low temperatures there is a stronger dependence on plasma density that may have to be accounted for. A study of the mechanism in initially cold targets will be the subject of future work.

## Acknowledgments

The authors are grateful for the use of computing resources provided by Science and Technology Facilities Council's e-Science facility.

## References

[1] Santala M *et al* 2000 *Phys. Rev. Lett.* **84** 1459
[2] Stephens R *et al* 2004 *Phys. Rev.* E **69** 066414

[3] Gremillet L *et al* 1999 *Phys. Rev. Lett.* **83** 5015
[4] Pisani F *et al* 2000 *Phys. Rev.* E **62** R5927
[5] Green J S *et al* 2007 *Nature Phys.* **3** 853
[6] Lancaster K *et al* 2007 *Phys. Rev. Lett.* **98** 125002
[7] McKenna P *et al* 2007 *Phys. Rev. Lett.* **98** 145001
[8] Kodama R *et al* 2004 *Nature* **432** 1005
[9] Kemp A J, Pfund R E W and Meyer ter Vehn J 2004 *Phys. Plasmas* **11** 5648
[10] Davies J R 2002 *Phys. Rev.* E **65** 026407
[11] Mason R J 2006 *Phys. Rev. Lett.* **96** 035001
[12] Honrubia J J, Antonicci A and Moreno D 2004 *Laser Part. Beams* **22** 129
[13] Bell A R, Robinson A P L, Sherlock M, Kingham R J and Rozmus W 2006 *Plasma Phys. Control. Fusion* **48** R37–57
[14] Davies J R, Green J S and Norreys P A 2006 *Plasma Phys. Control. Fusion* **48** 1181
[15] Davies J R 2003 *Phys. Rev.* E **68** 056404
[16] Tikhonchuk V 2002 *Phys. Plasmas* **9** 1416–21
[17] Tabak M *et al* 1994 *Phys. Plasmas* **1** 1626
[18] Hegelich M *et al* 2006 *Nature* **439** 441
[19] Schwoerer H *et al* 2006 *Nature* **439** 445
[20] Park H-S *et al* 2006 *Phys. Plasmas* **13** 056309
[21] Sentoku Y *et al* 2000 *Phys. Plasmas* **7** 689
[22] Honda M, Meyer ter Vehn J and Pukhov A 2000 *Phys. Rev. Lett.* **85** 2128
[23] Macchi A *et al* 2003 *Nucl. Fusion* **43** 362
[24] Hill J M *et al* 2005 *Phys. Plasmas* **12** 082304
[25] Califano F, Pegoraro F and Bulanov S V 1997 *Phys. Rev.* E **56** 963
[26] Bret A, Firpo M-C and Deutsch C 2005 *Phys. Rev. Lett.* **94** 115002
[27] Bret A and Deutsch C 2005 *Phys. Plasmas* **12** 102702
[28] Gremillet L *et al* 2002 *Phys. Plasmas* **9** 941
[29] Wilks S C and Kruer W L 2000 *IEEE J. Quant. Elec.* **33** 1954
[30] Robinson A P L and Sherlock M 2007 *Phys. Plasmas* **14** 083105
[31] Bell A R and Kingham R J 2003 *Phys. Rev. Lett.* **91** 035003
[32] Beg F N *et al* 1997 *Phys. Plasmas* **4** 447–57
[33] Green J S *et al* 2008 *Phys. Rev. Lett.* **100** 015003
[34] Lee Y and More R M 1984 *Phys. Fluids* **27** 1273